FEMTOSECOND LASER PHOTOELECTRON SPECTROSCOPY ON ATOMS AND SMALL MOLECULES: Prototype Studies in Quantum Control

M. Wollenhaupt,[1] V. Engel,[2] and T. Baumert[1]

[1]Institut für Physik, Universität Kassel, D-34132 Kassel, Germany;
email: wollenhaupt@physik.uni-kassel.de, tbaumert@physik.uni-kassel.de
[2]Institut für Physikalische Chemie, Universität Würzburg, D-97074 Würzburg,
Germany; email: voen@phys-chemie.uni-wuerzburg.de

Key Words multiphoton ionization, strong field excitation, coherent control, wavepacket dynamics

■ **Abstract** We review prototype studies in the area of quantum control with femtosecond lasers. We restrict this discussion to atoms and diatomics under gas-phase collision-free conditions to allow for a comparison between theory and experiment. Both the perturbative regime and the nonperturbative regime of the light-matter interaction are addressed. To that end, atomic/molecular beam techniques are combined together with femtosecond laser techniques and energy-resolved photoelectron spectroscopy and ion detection. Highly detailed information on the laser-induced quantum dynamics is extracted with the help of kinetic energy-resolved photoelectron spectroscopy.

1. INTRODUCTION

The ability to selectively steer quantum systems from an initial state $|i\rangle$ to any desired final state $|f\rangle$ with the help of suitably shaped light fields opens up undreamed-of prospects for applications in physics, chemistry, biology and engineering. This general field of quantum control, combined with the unique properties of lasers, has many different facets: A selected but by no means comprehensive list of examples includes applications in photochemistry (microscopic control of chemical reactions), quantum optics (optimized generation of high-harmonic soft X rays), atomic and molecular physics (wavepacket shaping and selective photo excitation), biophysics (optimization of nonlinear imaging techniques), solid-state physics (coherent current control) or applications in related quantum technologies (such as quantum computing or quantum cryptography). Specific examples can be found in References 1–10. Focusing on chemical

reaction dynamics, the timescale is determined by the atomic motions within their molecular frameworks and has been made accessible to experiment by the development of femtosecond laser technology during the past 20 years. Ultrashort light pulses can now be used to follow in real-time the primary events of many chemical but also physical or biological processes. The emerging field in the area of chemistry has been accordingly termed femtochemistry, and Ahmed Zewail received the Nobel Prize in Chemistry in 1999 "for his studies of the transition states of chemical reactions using femtosecond spectroscopy" (11, 12). The scope of the combination of quantum control with femtosecond laser techniques goes beyond simple observation, seeking to control chemical reactions (or more general quantum dynamics) by suitably shaped femtosecond light fields. Thereby it is possible to influence product distributions in such a way that the generation of desired products is enhanced, whereas the formation of unwanted by-products is simultaneously reduced. This is done directly in the investigated molecule by steering the dynamical evolution of quantum wave functions into the desired direction. It turns out that the manipulation of the interferences of matter waves is the key ingredient of quantum control. A number of recent review articles and books have treated the subject of quantum control from different perspectives (13–22). In order to get a better physical insight into different control scenarios it is essential to investigate specific control schemes on simple well defined model systems using well characterized femtosecond laser pulses to allow for a direct comparison between theory and experiment. The purpose of this review is to summarize recent efforts to selectively influence atomic and molecular dynamics with the help of (shaped) ultrashort laser pulses and to monitor the credibility of the system under consideration via photoelectron spectroscopy. This is an ambitious task, and the outcome of a satisfactory complete review would fill an entire series of books. Accordingly, we first define the frame of topics to be covered here, before we give examples from recent work.

1. We concentrate on atomic/molecular beam experiments, i.e., we restrict ourselves to atoms and molecules under gas-phase collision-free conditions.

2. As for the molecules, only diatomic molecules are considered. This means that the degrees of freedom of the systems are restricted to the electronic dynamics, a single vibrational nuclear coordinate, and an overall rotation. Here we consider time intervals for which the rotational degree of freedom can be assumed to be frozen.

3. The pulses discussed here have a typical duration of a few tens of fs and are further characterized by their frequency distribution, polarization vector, and intensity. Concerning the latter quantity, one might distinguish three regimes as follows:

   (*a*) Weak field limit. Here the population of the initial eigenstate—describing the system without the perturbation—can be treated as constant during the interaction introduced by the external field, i.e., we consider the perturbative limit.

(*b*) Strong fields. The field is intense enough so that an essential depopulation of the initial state occurs. This gives rise to temporal oscillations in the population of the participating electronic states, i.e., Rabi oscillations.

(*c*) Ultra-intense fields. The applied field is strong enough to induce multiple ionization and/or Coulomb explosion, above threshold ionization/ dissociation, generation of higher-order harmonics, etc. From the above-mentioned cases we treat only (*a*) and (*b*).

Because of the spectral width of the ultra-short pump–pulse, in general, a coherent superposition of eigenstates of the system is prepared. In an atom these states are of electronic character, whereas in a molecule they are eigenfunctions with respect to the electronic and nuclear degrees of freedom.

In pump-probe experiments, the (pump) pulse excitation is followed by an interaction with a second time–delayed (probe) pulse. This then yields different signals, e.g., transient absorption (where the modification of the probe-pulse due to the nonstationary behavior of the system is measured), or a fluorescence yield, which is recorded as a function of the pump-probe delay. Alternatively, one might also use time-resolved four-wave-mixing techniques (23, 24). In our case the probe step involves the ionization of the system, and the signal is the photoelectron kinetic energy distribution detected as a function of the pulse–delay, i.e., the time-resolved photoelectron (TRPE) spectrum. The application of TRPE-spectroscopy (TRPES) to polyatomic molecules and clusters has been extensively reviewed recently (25– 28) and extended to soft x-ray probing of the photodissociation of diatomics (29). Here we only briefly summarize the conceptual and practical advantages of TRPES: (*a*) Ionization is always an allowed process with relaxed selection rules due to the range of symmetries of the outgoing electron. (*b*) The final state in an ionization process is often a well-characterized state, which then serves as a template on which the evolving wavepacket is projected. (*c*) By differentially analyzing the outgoing electron with respect to kinetic energy and angular distribution, highly detailed information can be achieved. (*d*) In a simultaneous excitation and ionization experiment, the intermediate state leaves a fingerprint of the time evolution of its quantum mechanical phase in the photoelectron spectrum. (*e*) Detection of charged particles is extremely sensitive. (*f*) In combination with ion detection, mass information on the origin of the electron spectrum is achieved. Coincidence techniques are especially helpful in unraveling complex photodissociation dynamics.

This review is organized as follows: We start with an outline of the theoretical background, which is needed to understand the interaction of atoms and molecules with ultrashort pulses and the basics of time-resolved photoelectron spectroscopy. First, phenomena occurring in weak fields are discussed. These involve interference effects of free electron wavepackets, the imaging of vibrational wavepackets and dipole moments as well as control schemes relying on tailored laser pulses. In the second group, the strong field limit (in the sense as defined above) is treated, and it is shown how intense fields allow for the control of atomic and molecular ionization processes.

2. THEORY

For the systems defined above, the quantum treatment of pump–probe spectroscopy is based on the solution of the time-dependent Schrödinger equation (30–32). In the case of an ionization process, the exact incorporation of the ionization continuum is rather demanding. However, if one is not interested in photoelectron angular distributions (PADs) (33)—which have been recently exploited in the connection with time-resolved spectroscopy by several groups, both experimentally (34, 35) and theoretically (36–40)—but rather in the energy distribution of the electrons, simplified theories may be employed. They originate in the work of Seel & Domcke (31, 41, 42) and have been applied by us to describe various experiments, as is discussed below.

We first specify the molecular and interaction Hamiltonian. Then, weak field interactions are treated, and it is shown how wavepackets are prepared and can be detected via TRPES. The strong-field excitation will be treated separately.

2.1. Hamiltonian

We consider molecules, noting that the atomic case can be easily derived from the established formulation. Because no interaction is present between the quantum system and the environment, except for the interaction with the electromagnetic fields, the molecular Hamiltonian of the particles is given by the system Hamiltonian as

$$H^{(0)} = \sum_n |n\rangle \, H_n(R) \, \langle n| + \sum_\alpha \int dE \, |E, \alpha\rangle \, H_{E,\alpha}(R) \, \langle E, \alpha|, \qquad 1.$$

where $\{|n\rangle\}$ denotes a set of bound electronic states and $H_n(R)$ are the Hamilton operators for the nuclear motion, depending on the nuclear coordinates $\{R\}$. The system Hamiltonian contains a continuum part, where $|E, \alpha\rangle$ is the state of a photoelectron with energy E and a set of quantum numbers α. The operator $H_{E,\alpha}(R)$ describes the nuclear motion in the ionic core corresponding to the ejection of an electron characterized by the state $|E, \alpha\rangle$.

The interaction with the external field, within the dipole approximation, is

$$W(t) = -\sum_{n,m} |n\rangle \, \vec{\mu}_{nm}(R)\vec{E}(t) \, \langle m| - \sum_{n,\alpha} \int dE \, |E, \alpha\rangle \vec{\mu}_{n\alpha}(R, E)\vec{E}(t) \, \langle n|. \quad 2.$$

Here $\vec{\mu}_{nm}(R)$ denotes a transition dipole moment in the case $n \neq m$ and the permanent dipole moment for $n = m$. Note that the dipole moments, in general, depend on the nuclear coordinates R and the neutral-to-ionic transition depends on the photoelectron properties, i.e., on E and the quantum numbers α. Because we are not concerned with differential cross sections involving different states with quantum numbers α here, we will drop this index, so that the photoelectron states are labeled by their energy.

Equation 2 contains field-induced couplings between neutral states and between neutral and ionic states. Continuum-continuum couplings, on the other hand, are

neglected. Thus, effects like above-threshold ionization (43) or above-threshold dissociation (44) are neglected.

The temporal variation of the electric field of a pump–probe sequence that determines the interaction energy is given as

$$\vec{E}(t) = \vec{\epsilon}_1 \; f_1(t - T_1) \; \cos[\omega_1(t - T_1) + \phi_1(t - T_1)]$$
$$+ \; \vec{\epsilon}_2 \; f_2(t - T_2) \; \cos[\omega_2(t - T_2) + \phi_2(t - T_2)], \qquad 3.$$

where $\vec{\epsilon}_i$ are the polarization vectors, $f_i(t - T_i)$ are the pulse-envelope-functions centered at times T_i, ω_i are the carrier frequencies, and $\phi_i(t - T_i)$ are the temporal phase functions for pump- $(i = 1)$ and probe-pulse $(i = 2)$, respectively. The frequency distribution of the field appears in the Fourier expansion as

$$\vec{E}(t) = \frac{1}{2\pi} \int d\omega \; \vec{E}(\omega) \; e^{i\omega t} \qquad 4.$$

with

$$\vec{E}(\omega) = |\vec{E}(\omega)| e^{i\varphi(\omega)}, \qquad 5.$$

where $\varphi(\omega)$ describes the spectral phase function (45, 46).

2.2. Wavepackets

Regarding a one-photon absorption process initiated by a pump-pulse (unchirped) from the electronic ground state $|0\rangle$, the nuclear wave function in the electronic state $|1\rangle$ obtained after the interaction at $t = 0$ can be evaluated using perturbation theory as:

$$\psi_1(R, 0) = -\frac{1}{2i\hbar} \int\limits_{-\infty}^{\infty} dt \; U_1(-t) \; \vec{\mu}_{10}\vec{\epsilon}_1 \; f_1(t - T_1) \; e^{-i(E_{00} + \hbar\omega_1)t/\hbar} \; \psi_0(R). \quad 6.$$

Here $\psi_0(R)$ is the initial vibrational ground state of energy E_{00}, and $U_1(t)$ is the propagator in state $|1\rangle$ containing the nuclear Hamiltonian H_1. For an ultra-short pump-pulse, where the spectral width is accordingly broad and contains frequencies that are in resonance with several excited state eigenenergies, the wave function $\psi_1(R, 0)$ is a wavepacket, i.e., a coherent superposition of eigenfunctions. This is seen by expanding the wave function in the complete set of eigenfunctions $\{\varphi_{1,n}(R)\}$ in state $|1\rangle$ fulfilling the time-independent Schrödinger equation

$$H_1 \; \varphi_{1,n}(R) = E_{1n} \; \varphi_{1,n}(R). \qquad 7.$$

Assuming that only bound states are excited, this yields

$$\psi_1(R, t) = U_1(t)\psi_1(R, 0) = \sum_n \varphi_{1,n}(R) \; e^{-iE_n t/\hbar} \; d_n \; c_n(\omega_1), \qquad 8.$$

with the overlap integrals

$$d_n = \int dR \; \varphi_{1,n}(R) \; \vec{\mu}_{10}(R) \; \vec{\epsilon}_1 \; \psi_0(R), \qquad\qquad 9.$$

and the Fourier integrals

$$c_n(\omega_1) = -\frac{1}{2i\hbar} \int\limits_{-\infty}^{\infty} dt \; f_1(t - T_1) \; e^{i(E_{1n} - E_{00} - \hbar\omega_1)t/\hbar}. \qquad 10.$$

Thus, the wavepacket is indeed a superposition state, where the weights are determined by the molecular properties (d_n) and the pulse characteristics $c_n(\omega_1)$. Note that, in the cw-limit, the Fourier integral becomes proportional to a δ-function so that, for resonant excitation ($E_{1n} = E_{00} + \hbar\omega_1$), a single stationary state is excited.

Because of the time-dependent phase factors appearing in the expansion (Equation 8), the probability density $\rho_1(R, t) = |\psi_1(R, t)|^2$, i.e., the wavepacket, changes its position in coordinate space as a function of time (see Section 3.2).

2.3. Photoelectron Spectra

One central point in this review is the demonstration of the connection between the dynamics of radial wavepackets (see Section 2.2) and the TRPE-spectrum. To illustrate this relationship, it is sufficient to regard a one-photon ionization process taking place at a time delay $\tau = T_2 - T_1$, originating from the initial state $\psi_1(R, t)$. Assuming that the probe laser does not have a temporal overlap with the pump-pulse, first-order perturbation theory can be applied again to calculate the final state after the probe-pulse interaction at time τ as

$$\psi_E(R, \tau) \sim \int\limits_{-\infty}^{\infty} dt \; U_E(-t) \; \vec{\mu}_{E1}(R) \; \vec{\epsilon}_2 \; f_2(t - T_2) \; e^{-i\omega_2 t} \; \psi_1(R, \tau). \qquad 11.$$

The latter nuclear wave function corresponds to the ejection of an electron having energy E. The photoelectron spectrum, taken as a function of the pulse delay τ and of the kinetic energy E, is now determined as

$$P(E, \tau) = \langle \psi_E(R, \tau) | \psi_E(R, \tau) \rangle, \qquad\qquad 12.$$

where the brackets denote integration over the nuclear coordinate R.

The calculation of the TRPE-spectrum, taking all degrees of freedom of the ejected electron into account, is very involved (36–40). An essential simplification is obtained under the assumption that the photoelectron decouples from the nuclei and the other electrons. In that case, the total wave function separates into a product and the photoelectron energy enters as an additive constant into the nuclear Hamiltonian of the ionic state.

In order to establish the relation between the wavepacket $\rho_1(R, \tau) = |\psi_1(R, t)|^2$ and the spectrum $P(E, \tau)$, we assume that, during a femtosecond ionization,

the nuclei do not move substantially. Then, it is acceptable to neglect the kinetic energy operators appearing in the expression for the wave function of Equation 11 to obtain (47)

$$\psi_E(R, \tau) \sim \vec{\mu}_{1E}(R) \, \vec{\epsilon}_2 \, c_E(R, \omega_2) \, \psi_1(R, \tau),$$ 13.

with the Fourier integral

$$c_E(R, \omega_2) = \int\limits_{-\infty}^{\infty} dt f_2(t - T_2) \, e^{i(V_I(R) - V_1(R) - (\hbar\omega_2 - E))t/\hbar},$$ 14.

where $V_1(R)$ and $V_I(R)$ denote the potential energies in the neutral and ionic electronic state, respectively. The photoelectron spectrum now takes the form

$$P(E, \tau) = \int dR \, \rho_1(R, \tau) \, |\vec{\mu}_{1E}(R)\vec{\epsilon}_2|^2 \, |c_E(R, \omega_2)|^2.$$ 15.

(For an extensive discussion, see Reference 48). Here, it is sufficient to note that the window function $|c_E(R, \omega_2)|^2$ is, in general, a localized function of R, which assumes its maximum at points $R = R_i$, where the resonance condition

$$D_{I1}(R) - (\hbar\omega_2 - E) = [V_I(R) - V_1(R)] - (\hbar\omega_2 - E) = 0$$ 16.

holds. This result is in accordance with Mulliken's classical difference potential analysis (49–51). Here, it is due to the time-dependence of the phase factor appearing under the integral equation (Equation 14), which oscillates rapidly for distances R not fulfilling Equation 16. Because in the latter case, positive and negative contributions to the time-integral cancel out, the radial integral in Equation 15 is dominated by the contributions stemming from distinct points $R = R_i$. For a linear difference potential $D_{I1}(R)$, the photoelectron spectrum at a fixed energy E is directly proportional to the radial density times the projection of the transition dipole moment at that value of the internuclear distance $R = R_i$, which is fixed via the resonance condition (Equation 16), i.e.,

$$P(E, \tau) \sim \rho_1(R, \tau) \, |\vec{\mu}_{1E}(R)\vec{\epsilon}_2|^2.$$ 17.

However, this concept is generally applicable for nonlinear monotonic difference potentials as well. Equation 17 has two important implications: (*a*) the detection of a TRPE-spectrum allows one to monitor spatial changes of the wavepacket, and (*b*) if the transition dipole moment shows a substantial dependence on the nuclear coordinate R, it is possible, via a comparison of measured and calculated spectra, to determine such a dependence from the measured spectrum. Below, we address both points in more detail.

2.4. Strong Field Excitation

In this subsection, we treat the excitation with a strong field that is able to essentially depopulate the initial state. Thus, perturbation theory fails and the Schrödinger

equation for the nuclei in different electronic states, which are coupled by the external field, has to be integrated numerically. Let us, as an example, discuss the interaction of a single ultra-short pulse with a molecule, assuming that three electronic states and an ionization continuum participate in the excitation process. In what follows, we treat only the strong field coupling between the neutral states, whereas the coupling to the ionization continuum is described within perturbation theory. This is a good approximation in the cases we regard below. The nuclear wave functions are then determined by the following set of equations:

$$i\hbar \frac{\partial}{\partial t} \begin{pmatrix} \psi_0 \\ \psi_1 \\ \psi_2 \end{pmatrix} = \begin{pmatrix} H_0 & W_{01} & 0 \\ W_{10} & H_1 & W_{12} \\ 0 & W_{21} & H_2 \end{pmatrix} \begin{pmatrix} \psi_0 \\ \psi_1 \\ \psi_2 \end{pmatrix} \qquad 18.$$

$$\psi_E(R, t) \sim \int_{-\infty}^{t} dt' \, U_E(t - t') \, W_{E2}(t') \, \psi_2(R, t), \qquad 19.$$

where we included couplings between neighboring neutral electronic states ($n - n' = \pm 1$);

$$W_{nn'}(R, t) = -\vec{\mu}_{nn'}(R)\vec{\epsilon}_1 \, f(t) \cos(\omega t + \phi(t)); \qquad 20.$$

and the couplings of upper state with a continuum state of energy E:

$$W_{E2}(R, t) = -\vec{\mu}_{E2}(R)\vec{\epsilon}_1 \, f(t) \cos(\omega t + \phi(t)). \qquad 21.$$

The working equations, provided in this section, are sufficient to analyze the various examples described below.

3. QUANTUM CONTROL IN THE WEAK FIELD LIMIT

3.1. Free Electron Wavepackets

After the pioneering electron diffraction experiments of Davisson & Germer (52), which demonstrated the wave properties of matter, interferences of matter waves have been among the most successful confirmations of the wave–particle dualism (53). The first evidence of spatial electron interferences is given in a Young's double slit experiment (54). In addition to the fundamental aspect of emphasizing the wave character of a particle, an interference experiment provides a tool of ultrahigh sensitivity that is often used to probe matter properties.

In this section we start our discussion by investigating the interference of free electron wavepackets created by the ionization of excited state ($5p$) potassium atoms using a pair of two time-delayed ultrashort laser pulses. During the time evolution of the free electrons, the wavepackets interfere and the interference fringes are measured with a time-of-flight (TOF) electron detector.

The presented experiment demonstrates the coherence transfer from light pulses to free electron wavepackets. This will allow employing the highly developed technology of pulse shaping to manipulate matter waves in a similarly flexible fashion. The prospect to spatially focus electron wavepackets at a given target may significantly stimulate, for example, experiments on time-resolved electron diffraction (55) and the experiments on electron recollision (56). Moreover, the technique can be employed for the characterization of shaped laser pulses in the XUV spectral region and beyond, where pulse characterization methods are strongly demanded.

The experiment is described in detail in Reference (57) and therefore is only briefly sketched in Figure 1*a*. We specialize the theory given in Section 2 for the molecular case to atomic transitions. This is formally carried out by fixing the bond length R to a constant and performing the following replacements in Equation 11:

$$\psi_1(R, t) = e^{-iE_{5p}t/\hbar}\, c(5p), \quad U_E(t) = e^{-i(E_{IP}+E)t/\hbar}, \quad \vec{\mu}_{E1}\vec{\epsilon}\, f(t)\, e^{-i\omega t} = W(t),$$
22.

where the amplitude in the initial state is $c(5p) = 1$. In what follows, we refer to the product $W(t)$ as an electric field. We then obtain for the amplitude of the photoelectron state after the pulse interaction

$$c(E) \propto \int_{-\infty}^{\infty} dt\, e^{i(E+E_{IP}-E_{5p})t/\hbar}\, W(t).$$
23.

The laser field couples the initially prepared $5p$ state (energy $E_{5p} = 3.06\,\text{eV}$) to the continuum level with energy $E + E_{IP}$, where E_{IP} denotes the ionization potential of the atom. Ionization from the $5p$ state with one 790 nm photon (1.58 eV) delivers photoelectrons around $E = 0.3\,\text{eV}$ kinetic energy because of the ionization potential of $E_{IP} = 4.34\,\text{eV}$. The photoelectron spectrum, measured in eV, is now obtained as

$$P(E) = |c(E)|^2 \propto |\tilde{W}(E + E_{IP} - E_{5p})|^2 = PSD(E + 1.28\,\text{eV}),$$
24.

i.e., the photoelectron spectrum $P(E)$ is proportional to the power spectral density (PSD) of the driving electric field at the photon frequency $\omega_{ph} = [E + E_{IP} - E_{5p}]/\hbar$.

In the experiment, a pair of two time-delayed ultrashort laser pulses characterized by the electric field $W'(t) = W(t) + W(t - \tau)$ is used to generate a coherent double-peaked free electron wavepacket in the ionic continuum. Therefore, we write the amplitudes, according to Equation 23, making use of the Fourier shift theorem,

$$c'(E) \propto (1 + e^{i\omega_{ph}\tau})\tilde{W}(\omega_{ph}),$$
25.

and obtain for the photoelectron spectrum of the pulse pair

$$P(E) \propto [1 + \cos(\omega_{ph}\tau)]\, PSD\,(E + 1.28\,\text{eV}).$$
26.
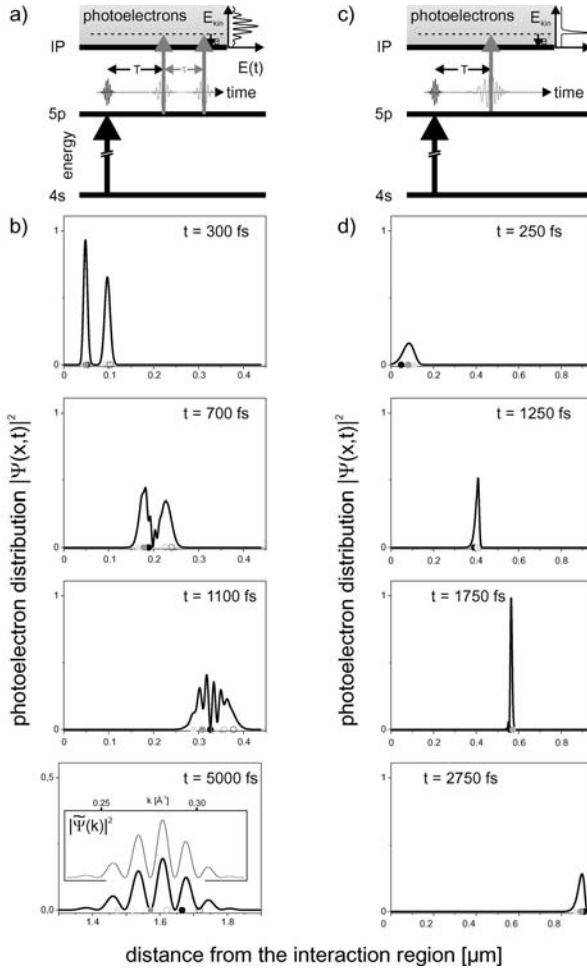
Figure 1 Energy levels for the excitation/ionization of potassium atoms. (*Left column*) Double pulse experiment as measured, (*right column*) chirped pulse ionization. (*a*) With a 405 nm femtosecond laser pulse the atom is prepared in the $5p$ state. After a fixed delay (T) of 3 nanoseconds, the 790 nm pulse pair generates a coherent double-peaked free electron wavepacket with an excess energy of about 0.3 eV. (*b*) Time evolution of the electron wavepackets generated by the ionization with two 785 nm, 25 fs pulses separated by $\tau = 150$ fs. The position of the classical electrons with a kinetic energy of $E - \frac{\hbar \Delta \omega_l}{2}$ (*light gray*), E (*gray*), and $E + \frac{\hbar \Delta \omega_l}{2}$ (*black*) is indicated with *open circles* for the first pulse and *filled circles* for the second pulse. For t = 5000 fs a comparison with the stationary momentum distribution $|\tilde{\psi}(k)|^2$ is shown. (*c*) Excitation scheme for chirped pulse ionization. (*d*) Time evolution of an electron wavepacket created by the ionization with an up-chirped ($\Phi = 2000$ fs^2) 785 nm, 25 fs laser pulse. The wavepacket reaches its maximum localization at around 1750 fs. The positions of the slow, central, and fast classical photoelectrons are indicated with *light gray circles*, *gray circles*, and *black filled circles*, respectively.

From Equation 26, we expect the photoelectron signal at a given photoelectron energy to sinusoidally oscillate as a function of the pulse delay time τ with the photon frequency. Likewise, at a fixed delay time τ, fringes in the photoelectron spectrum with an energy separation of h/τ should be visible. Hence, varying the temporal delay between the pair of ionizing laser pulses changes the interference pattern in the photoelectron spectrum. By recording the energetically resolved photoelectron signal as a function of the time delay, the structure of tilted ellipses as shown in Figure 2a and 2c, shows up. We note that the same effect is obtained in the case of the fragmentation of a diatomic molecule induced by two time-delayed pulses. There, the fringes appear in the fragment kinetic energy distributions (58), and tomographic reconstruction of the quantum state was reported on the I_2 molecule. For early development times the double-peaked wavepacket structure has been observed via Coulomb explosion techniques (59).

The electron wavepacket $\psi(x, t)$ (after the pulse interaction) is the superposition of the plane waves $\psi_E(x, t)$ with the amplitudes $c(E)$ from Equation 23;

$$\psi(x, t) = \frac{1}{\sqrt{2\pi}} \int\limits_{0}^{\infty} dE \, c(E) e^{i(k_E x - Et/\hbar)} = \frac{1}{\sqrt{2\pi}} \int\limits_{-\infty}^{\infty} dk \, \tilde{\psi}(k) \, e^{i\left(kx - \frac{\hbar k^2}{2m_e}t\right)}, \quad 27.$$

where we employed the dispersion relation $k_E = \sqrt{2m_e E}$ and identified $\tilde{\psi}(k) \, dk = c(E) \, dE$. Here $|\tilde{\psi}(k)|^2$ describes the momentum distribution of the electron wavepacket. In momentum space, the time evolution after the creation of the wavepacket is described by the phase factor $e^{-i\frac{\hbar k^2}{2m_e}t}$, implying that the momentum distribution $|\tilde{\psi}(k)|^2$ is stationary.

Next, we consider the spatio-temporal evolution of the double-peaked wavepacket as depicted in Figure 1b for two 25 fs *FWHM*, 790 nm Gaussian laser pulses with a delay τ of 150 fs. The first electron wavepacket is generated by the interaction of the first pulse. The spatial shape of the wavepacket is similar to the temporal shape of the pulse. An identical partial wavepacket is generated during the interaction with the second laser pulse, which is seen at 300 fs and therefore at the end of the laser interaction; the outward moving electron wavepacket exhibits a double-peaked structure similar to the exciting laser pulse pair slightly distorted by dispersion. The dispersion reduces the height of the wavepacket and broadens the distribution in space. Progressing dispersion spreads the partial wavepackets leading to an overlap of the partial wavepackets, which gives rise to the transient interference structures shown in Figure 1b at 700 to 1100 fs. This is the case when the blue classical photoelectrons generated by the second pulse reach the red classical photoelectrons of the first wavepacket. Then, the fast components of the second wavepacket overtake the slow components of the first wavepacket until the relative sequence of the colors is stationary. At approximately 5000 fs the shape of the wavepacket is quasistationary, which means that it still broadens and reduces its height but the shape is conserved. Indeed, the shape of the wavepacket eventually converges to the photoelectron spectrum taken on a spatial scale, i.e., the probability distribution $|\psi(x)|^2$ in coordinate space converges to the
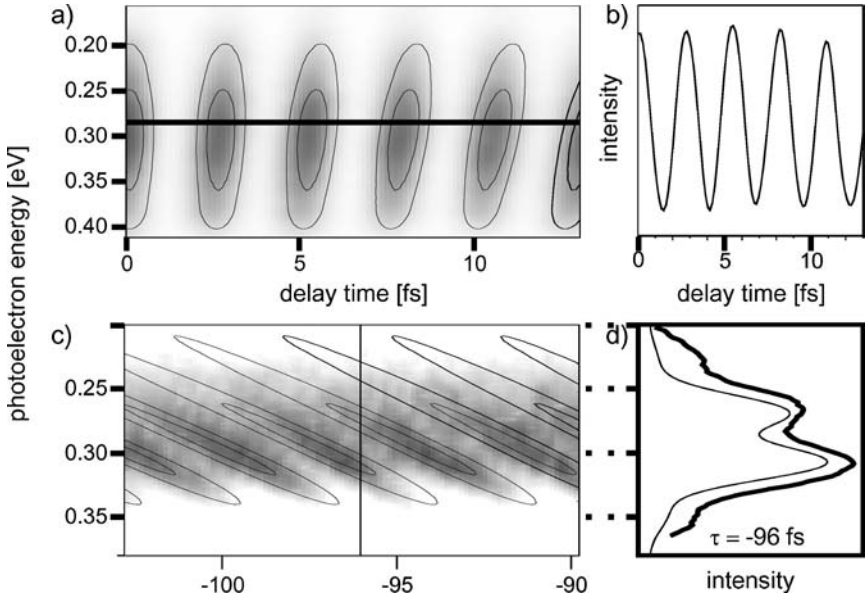
Figure 2   Experimental results for threshold electrons around zero (*a*) and around 100 fs (*c*) delay time τ. For comparison, calculated contours are superimposed. (*b*) A section along the time-delay axes at fixed energy indicates oscillatory behavior with varying time delay. (*d*) Section along the photoelectron energy axes at $\tau = -96$ fs showing fringes in the measured photoelectron spectrum (*bold*). A calculated spectrum convoluted with 25 meV spectrometer resolution is given for comparison.

momentum distribution $|\tilde{\psi}(k)|^2$ measured in coordinate space. This is clearly seen in Figure 1*b* at 5000 fs by comparison of the wavepacket $|\psi(x, t = 5000 \text{ fs})|^2$ and the stationary momentum distribution $|\tilde{\psi}(k)|^2$ on top.

The energy spectrum of the released photoelectrons was recorded as a function of the delay time τ between the two 790 nm laser pulses. Electrons at threshold energy show a periodic intensity modulation at the laser frequency, with varying delay time resulting in the ellipses displayed in Figure 2 for short delay times (Figure 2*a*) and for delay times at which the laser pulses are well separated in time (Figure 2*c*) so that no optical interferences occur. The results agree well with the calculated intensity profile also displayed in Figure 2. For the calculation (using Equation 26) the measured PSD and time delay were adopted. To quantify the experimental results the fringes in the photoelectron spectrum could be directly compared to simulated spectra as demonstrated in Figure 2*d*. In this comparison, the resolution of the spectrometer (25 meV) was taken into account.

Above we saw that the wavepacket melts away owing to the dispersion. In what follows, we investigate whether we can precompensate the dispersion of matter waves by suitable choice of the sequence of the spectral components within the laser pulse. Chirped pulses deliver a frequency sweep during the pulse and are therefore suitable candidates to focus a wavepacket as depicted in Figure 1*c*.

Figure 1*d* shows the time evolution of an electron wavepacket created by the ionization from the $5p$ excited state of potassium atoms with an up-chirped 785 nm, 25 fs laser pulse with a bandwidth of $\Delta\omega_l = 0.11$ fs^{-1} corresponding to 36.2 nm, where the chirp parameter Φ was set to 2000 fs^2. Because up-chirped laser pulses start with the red components, i.e., the low energy part of the photoelectron spectrum of the wavepacket, the red components appear before the blue components. The coordinates of the classical electrons are plotted as *filled circles* in Figure 1*d*. We can use the crossing of classical trajectories to estimate the time of the peak intensity of photoelectrons as

$$t_{peak} = 2\Phi E/\hbar, \tag{28.}$$

which evaluates to $t_{peak} \approx 1820$ fs for the above conditions. Because of the dispersion relation of matter waves, the group velocity increases with k and therefore the blue components travel faster than the red ones in agreement with the classical velocities. As the blue components catch up with the red ones (Figure 1*d* at around 1250 fs), the wavepacket piles up. At around 1750 fs the blue components start to overtake the red ones at approximately 0.6 μm, giving rise to the highly localized photoelectron peak.

3.2. Vibrational Wavepacket Imaging

In Section 2.3, we established the relationship between the time-dependent probability density of a wavepacket created in a pump-process and the time-resolved photoelectron spectrum. This connection was first illustrated in the seminal work of Seel & Domcke (41, 42) who studied the multimode vibrational dynamics of pyrazine and showed how the nuclear dynamics is reflected in temporal variations of the photoelectron spectrum.

We calculated the TRPE-spectrum for a three-photon ionization process in the Na$_2$ molecule (60), where the relationship between the dynamics of a single vibrational mode and the spectrum is unique. The excitation scheme is displayed in Figure 3*a*. Here, starting from the electronic ground state $X^1\Sigma_g^+$, a pump pulse prepares vibrational wavepackets in the excited $A^1\Sigma_u^+$ state via a one-photon transition and also in the $2^1\Pi_g$ state via a two-photon transition. The time-delayed ionization produces photoelectrons with different kinetic energies E. Figure 3 also shows the difference potential between the ionic state $^2\Sigma_g^+$ and the $2^1\Pi_g$ state. According to the resonance condition (Equation 16) and Equation 17, this function establishes, for a given probe-pulse frequency ω_2, a unique mapping between the wavepacket and the TRPE-spectrum. This is illustrated in Figure 3, which shows the vibrational wavepacket in the Π-state (Figure 3*b*) and the photoelectron spectrum (Figure 3*c*), calculated for a constant dipole moment. Clearly, the motion of the localized wavepacket is mapped into the spectrum. Here, we are able to take a direct look at real-time changes of a quantum mechanical probability density that are reflected in the time-resolved photoelectron spectrum.
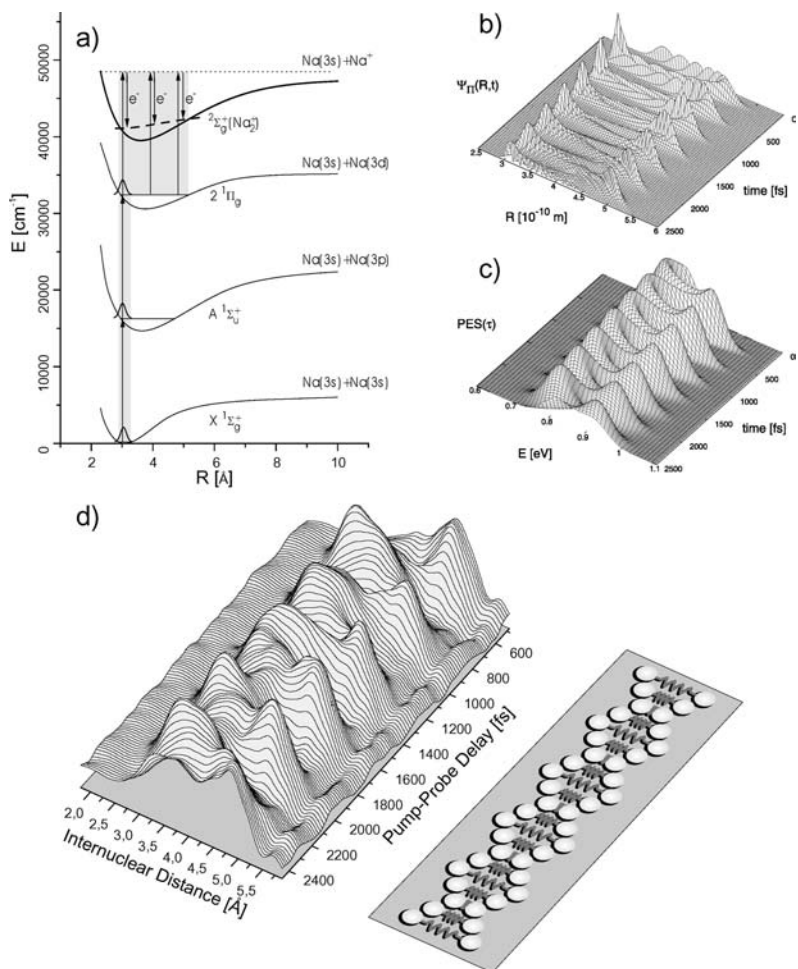
Figure 3 Mapping of vibrational wavepackets. (*a*) Excitation scheme for the Na_2 molecule. The pump laser in the range of 620 nm creates wavepackets in the $A^1\Sigma_u^+$ and the $2^1\Pi_g$ states at the inner turning points. The time-delayed probe laser ionizes the sodium dimer. As indicated, the kinetic energy of the photoelectrons depends on the internuclear coordinate because of the monotonic increasing difference potential (*dashed line*). (*b*) Wavepacket dynamics in the Π-state. Shown is the absolute square of the vibrational wavepacket created by a two-photon transition from the ground state at 620 nm. (*c*) The periodic motion is mapped into the photoelectron spectrum. The latter was calculated for a one-photon ionization out of the Π-state. (*d*) After calibration of the spectrometer with the help of atomic resonances, the measured time-of-flight axis is converted into an energy axis. Taking the difference potential into account (i.e., employing Equation 16), the mapped wavepacket dynamics as a function of the internuclear distance is obtained with sub-Å spatial resolution. The corresponding harmonic oscillation of a classical diatomic is shown for comparison.

The experiment that finally demonstrated wavepacket mapping was performed on the sodium dimer (51). Using the pump-probe ionization scheme as sketched in Figure 3a, the spectrum as displayed in panel d was obtained. Instead of plotting the kinetic energy of the photoelectrons, the energy was converted into a distance (61) employing Equation 16, which is a unique relation as the difference potential is an increasing function of the bond length R. The figure verifies that the application of TRPES allows for the observation of changes of the nuclear configuration of a molecule with sub-Å resolution. (See also References 62–65.)

3.3. Imaging Electronic Changes Using Vibrational Wavepackets

Measurements using ion detection have attempted to determine the ionization probability as a function of the internuclear separation in diatomics (66–69). However, because the ion signal is an electron energy–averaged quantity, these results are obscured by the potential presence of other ionization pathways. In this section, we report on an experiment in which the above restrictions are circumvented by the use of energy-resolved photoelectron detection. The photoelectron spectrum delivers an additional degree of freedom that is essential to unambiguously identify all of the ionization pathways. The idea of the experiment is to use a femtosecond pump laser pulse to create a highly localized wavepacket that samples a large range of internuclear separations. A probe pulse ionizes the molecule at the position of the wavepacket and thus locally measures the ionization dipole moment (the transition dipole moment for a neutral-to-ionic transition) as a function of the internuclear coordinate.

Using Equation 15, we assume that the potentials of the neutral and ionic electronic states as well as the laser parameters are known. Then, the nuclear densities $\rho_1(R, \tau)$, i.e., the vibrational wavepackets, and the window functions $I_E(R, \omega_2)$ can be calculated. If the spectrum for a fixed energy E is measured for a sufficiently large number of delay times τ_n, the radial integral in Equation 15 can be discretized; this results in a matrix equation with vectors $P(E, \tau_n)$, the projection of the transition dipole moment on the laser polarization $|\mu_{1E}(R_m)|^2$, and the matrix $|\rho_1(R_n, \tau_m)I_E(R_n, \omega_2)|^2$. The latter matrix equation may be inverted to directly yield the unknown absolute square of the dipole-moment function. (For a detailed analysis see Reference 70). In what follows, a simpler approach is applied to transitions in the Na_2 molecule. The relevant potential energy curves for $\lambda_{pump} = 340$ nm excitation of the Na_2 $2^1\Sigma_u^+$ double-minimum state (pump) and subsequent $\lambda_{probe} = 265$ nm ionization to the bound Na_2^+ $1^2\Sigma_g^+$ and repulsive Na_2^+ $1^2\Sigma_u^+$ ionic states (probe) are shown in Figure 4a. The Na_2 $2^1\Sigma_u^+$ state is an ideal candidate to study electronic changes along the internuclear coordinate because it arises from the avoided potential crossing of several adiabatic potentials (71–73). The inner potential well is characterized as a Rydberg-type state, whereas the outer potential well has more of an ionic character (72, 73). The adiabatic motion of a wavepacket on the double-minimum potential therefore probes regions of different electronic configurations. Because the neutral-to-ionic dipole moment μ is a sensitive probe
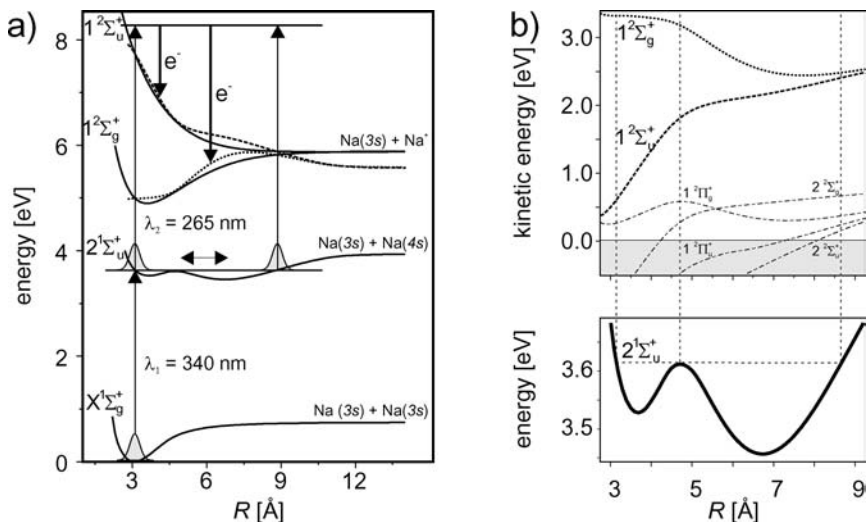
Figure 4 (*a*) Potential energy curves for $\lambda_{pump} = 340$ nm excitation of the Na$_2$ $2^1\Sigma_u^+$ double-minimum state (pump) and subsequent $\lambda_{probe} = 265$ nm ionization to the bound Na$_2^+$ $1^2\Sigma_g^+$ and repulsive Na$_2^+$ $1^2\Sigma_u^+$ ionic states (probe). The corresponding difference potentials for the bound (*dotted line*) and the repulsive (*dashed line*) ionic states are displayed. In the experiment, energy-resolved photoelectron spectra from both ionic states are measured. (*b*) Difference potentials of the Na$_2^+$ $1^2\Sigma_g^+$, $1^2\Sigma_u^+$, $1^2\Pi_g^+$, $1^2\Pi_u^+$, $2^2\Sigma_g^+$, and $2^2\Sigma_u^+$ ionic potentials, the Na$_2$ $2^1\Sigma_u^+$ potential for $\lambda_{pump} = 340$ nm excitation, and $\lambda_{probe} = 265$ nm ionization. The horizontal *dashed line* indicates the energy level above the barrier, the *vertical lines* indicate the electron energies at the inner turning point (*in*), the barrier (*ba*), and the outer turning point (*ou*).

for the electronic configuration, a change of the ionization probability along the internuclear coordinate is to be expected. Indeed, a strong variation of $\mu(R)$ was theoretically predicted for the Na$_2$ double-minimum state (37, 38). For ionization at 544 nm negligible ionization was predicted for the inner potential well, whereas an oscillating dipole moment was calculated for the barrier and the outer well (37). In a two-color 340 nm pump and 540 nm probe experiment, ions from the outer turning point were detected to obtain spectroscopic information for the Na$_2$ double-minimum state (74). Using kinetic energy time-of-flight mass spectroscopy in a one-color (341.5 nm) pump-probe scheme (75), the dynamics of the wavepacket on the Na$_2$ double-minimum state was mapped. Applying time-resolved photoelectron detection in another one-color (340 nm) pump-probe experiment has shown that the ionization at the outer turning point is favored, but no direct comparison with time domain simulations was performed (76).

At a wavelength of 340 nm the vibrational wavepacket on the Na$_2$ $2^1\Sigma_u^+$ state is excited above the barrier. Figure 5*a* shows the wavepacket motion for 340 nm, 35 fs
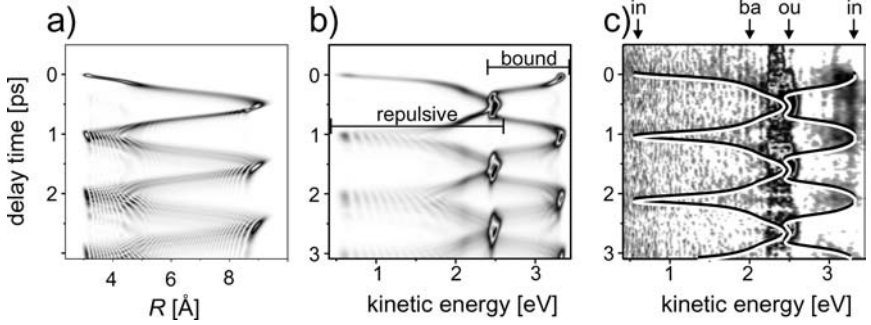
Figure 5 (*a*) Gray scale representation of the temporal evolution of the wavepacket on the Na$_2$ $2^1\Sigma_u^+$ state for λ_{pump} = 340 nm, *FWHM* = 35 fs excitation from the Na$_2$ X$^1\Sigma_g^+$ (v$''$ = 0) ground state. (*b*) Calculated photoelectron distribution assuming an R-independent ionization dipole moment. (*c*) Experimental result: photoelectron spectra as a function of the pump-probe delay. The classical photoelectron energies are plotted on top of the measurement to guide the eye.

pulsed laser excitation from the X$^1\Sigma_g^+$ (v$''$ = 0) state. Because the initial potential energy of the wavepacket is sufficient to overcome the barrier, the wavepacket performs (almost) unperturbed oscillations across the full $2^1\Sigma_u^+$ potential. Therefore, excitation at this wavelength is particularly suitable for the investigation of the electronic changes along the internuclear coordinate in a range of 3 to 9 Å.

We used the combination of classical trajectory and difference potential analysis, i.e., employing the resonance condition (Equation 16), to plot the classical results on top of the experimental results, which helps to identify the ionization pathway as shown in Figure 5*c*.

As seen in the difference potential in Figure 4*b*, ionic potentials other than the $1^2\Sigma_g^+$ and $1^2\Sigma_u^+$ potential can contribute to the measured signal as well. The difference potentials show that all contributions from these ionic states are mapped onto the energy interval of 0 to 0.7 eV and can therefore only interfere with electrons from the $1^2\Sigma_u^+$ state. Because significant contributions are only found when the wavepacket is located at the outer turning point, this nicely temporally separates these signals from the $1^2\Sigma_u^+$ photoelectrons in the low energy window, which are only emitted at the inner turning point at 0, 1, and 2 ps, etc. This means that, in our data, signals from higher-lying ionic states are not observed.

A detailed description of this experiment can be found in (77). Figure 5*c* shows a gray scale representation of the measured photoelectron spectra obtained within the first 3.5 ps time delay between pump- and probe-pulses compared with calculations in Figure 5*a* and 5*b*. To enhance the visibility of the measured signal the kinetic energy for classical electrons is superimposed as a *line* in Figure 5*c*. Note that the electrons from both ionic curves overlap at a kinetic energy of 2.5 eV. Photoelectrons from the repulsive (bound) ionic state appear in the energy interval

0.4–2.6 eV (2.4–3.5 eV). For the bound ionic potential, agreement between the observed photoelectrons and the calculations was achieved to first order for a linearly increasing dipole moment $\mu_b(R)$ of the form

$$\mu_b(R) = (0.14 \, \text{Å}^{-1} R + 0.36)\mu_0. \qquad 29.$$

The procedure for deriving the R-dependent dipole-moment function is described in (77). Because the ionization probability is proportional to the square of the dipole moment we find that for the bound ionic state the ionization probability at the outer turning point is $[\mu_b(8.8 \, \text{Å})/\mu_b(3.1 \, \text{Å})]^2 = 4.0 \pm 0.4$ times the ionization probability at the inner turning point. Moreover, at the outer turning point the ionization probability for the bound state is roughly $[\mu_b(8.8 \, \text{Å})/\mu_r(8.8 \, \text{Å})]^2 = 6.0 \pm 0.6$ times larger than the ionization probability for the repulsive state.

3.4. Molecular Chirped Pulse Excitation

Introducing a quadratic spectral phase function (see Section 2.1), i.e., a chirp, in the laser pulses leads to various effects and also results in the modification of the photoelectron spectrum (78). As an example, we consider a single pulse experiment on the Na_2 molecule, where the carrier frequency ω_0 is 618 nm, which is resonant with the electronic transitions as displayed in Figure 3a. In the experiment, starting from a Fourier-transform limited 40 fs pulse, either an up-chirp ($+3500 \, \text{fs}^2$) or a down-chirp ($-3500 \, \text{fs}^2$) is introduced. The photoelectron spectra for a three-photon ionization and for different chirps are displayed in Figure 6. As a first observation, the spectra are essentially modified by the introduction of a chirp. The appearance of the spectrum in each case can be explained by a detailed theoretical analysis (79). Therefore one must, on one hand, consider the Franck-Condon window for each electronic transition and the dynamics in the intermediate states, on the other. This, of course, makes the molecular system more complicated—and also more interesting—as compared with the atomic case where no vibrational dynamics in intermediate states is present. Here, we only discuss why a substantial broadening occurs upon the introduction of a chirp. Because the Π-state is directly coupled to the ionization continuum, the position and width of its vibrational wavepacket $\psi_\Pi(R, t)$ determines the appearance of the spectrum. (See Equations 16 and 17.) For an unchirped pulse of about 40 fs temporal duration, the latter wavepacket remains almost stationary during the ionization process, resulting in a rather compact photoelectron spectrum. The introduction of a chirp lengthens the pulse to about 240 fs, in the present case. As a consequence, the wavepacket is able to sample a larger interval of bond distances. Taking the resonance condition (Equation 16) and the linearly increasing difference potential between the Π-state and the ground state of Na_2^+ into account, this results in a broader range of energies E that are accessible, i.e., one observes a broadening of the spectrum as compared with the unchirped case.

   An interesting situation occurs when a chirped pulse ionization originates from a nonstationary state, here, a vibrational wavepacket. Because chirping leads to longer time-domain pulses, the motion of the wavepacket can no longer be ignored
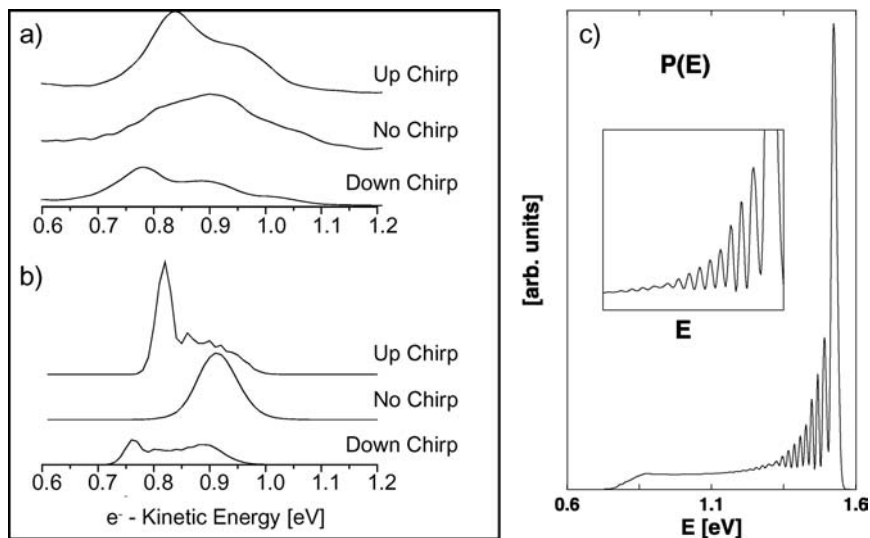
Figure 6 (*a*) Electron spectra measured with single up-chirped ($+3500$ fs^2), down-chirped (-3500 fs^2), and unchirped laser pulses. The transform-limited pulses of 40 fs duration are centered at a wavelength of 618 nm. The chirped pulses are of 240 fs duration. (*b*) Calculated spectra using the same parameters as above. Panel *c* shows a calculated photoelectron spectrum exhibiting interferences. The latter structures are shown on an enhanced scale in the inset. Here, the introduction of a chirp lengthens the pulse. If ionization occurs from a nonstationary state, electrons having kinetic energies within a certain range can be produced—owing to the vibrational motion—at different times, which produces the interference patterns in the spectrum.

during the ionization process. In particular, if the probe-pulse is timed such that it interacts with the system during times when the wavepacket is reflected at a potential wall, the following scenario appears: The ejection of an electron with a fixed energy E can occur at several distinct times. Because the photoelectron spectrum results from the coherent superposition of amplitudes for ionization at different times, each process leading to the same final state gives rise to interference patterns in the spectrum. The effect is illustrated in Figure 6*c*, which shows a spectrum obtained for the two-photon pump-probe ionization of Na$_2$, as was discussed in Section 3.3. Here we employed linearly up-chirped ($+6000$ fs^2) 50 fs Fourier transform–limited Gaussian pulses with wavelengths of 332 nm. At larger photoelectron energies, the spectrum exhibits fast oscillations with a separation of $\Delta E = 0.03$ eV. This corresponds to a time of $\Delta t = 2\pi\hbar/\Delta E = 137$ fs. An analysis of the wavepacket dynamics in the double-minimum state, together with the resonance condition for ionization (Equation 16), shows that the initial wavepacket passes the excitation window (responsible for the production of high-energy electrons) twice on its way inward and outward, where the time-difference is just about the calculated 137 fs. The large maximum and the decrease of the spectrum for

higher energies can be explained (80) in analogy to rainbow scattering occurring, e.g., in atom-atom scattering processes (81). Studies on rotational wavepacket quantum interferences with shaped ultrashort laser pulses were reported on the Li_2 prototype (82).

## 3.5. Quantum Control by Ultrafast Polarization Shaping

Conventional pulse shaping (83) is based on the manipulation of the scalar spectral phase function and therefore leaves the direction of the electric field vector unchanged. However, because the light matter interaction is described by the vectorial quantities $\vec{\mu} \cdot \vec{E}(t)$, the use of polarization as an additional control parameter could tremendously increase the degree of attainable control. Generally, this will be the case if the polarization state follows the molecular dynamics throughout the complete temporal evolution of a quantum system in order to maximize the population transfer. The experiment described in this section makes use of femtosecond polarization pulse-shaping techniques (84, 85) by which the polarization state of light (i.e., the degree of polarization ellipticity and orientation of elliptical principal axes) as well as the temporal intensity and the instantaneous oscillation frequency can be varied as functions of time within a single femtosecond laser pulse. The use of spectral modulation of the phase and the polarization direction was demonstrated in coherent anti-Stokes Raman spectroscopy (CARS) (86), on the multiphoton absorption of atomic Rubidium (87), and on the efficient production of evenly or oddly charged molecular ions from aligned I_2 molecules (88).

We use adaptive polarization shaping to maximize multiphoton ionization of potassium molecules K_2. The experiment is detailed in (89). At a laser wavelength of 785 nm, the dominant ionization pathway (K_2^+ $^2\Sigma_g^+$ $\leftarrow$ $2^1\Pi_g$ $\leftarrow$ $A^1\Sigma_u^+$ $\leftarrow$ $X^1\Sigma_g^+$) (67) starts with the population of the $A^1\Sigma_u^+$ state, intermediate wavepacket propagation on the $A^1\Sigma_u^+$ state, further excitation to the $2^1\Pi_g$ state, and ionization from the $2^1\Pi_g$ state as shown in Figure 7a.

Because the dipole moment $\mu_{\Sigma-\Sigma}$ of the $A^1\Sigma_u^+ \leftarrow X^1\Sigma_g^+$ transition is parallel to the internuclear axis ($\Delta\Lambda = 0$), and the dipole moment $\mu_{\Pi-\Sigma}$ of the $2^1\Pi_g \leftarrow A^1\Sigma_u^+$ transition is perpendicular to the internuclear axis ($\Delta\Lambda = 1$) as shown in the inset to Figure 7a, this pathway is strongly polarization dependent. As a consequence, we expect the optimal electrical field vector to rotate during the excitation process.

In the experiment the setup consists of a polarization pulse shaper that is controlled by a computer with an optimization algorithm in order to maximize the ionization process with pulses of optimal intensity profile and polarization state.

Figure 7b shows the experimental results of two types of adaptive control experiments to maximize the K_2^+ yield: spectral polarization-and-phase laser pulse shaping as well as phase-only shaping. For both cases the evolution of the K_2^+ signal as a function of generation is depicted in Figure 7b. The increase for phase-only pulse shaping (*black circles*) is due to the adaptation of the laser pulse structure to the vibrational dynamics of the potassium dimer. However, when the additional mechanism of light-polarization control is used (*gray disks*), a significantly higher
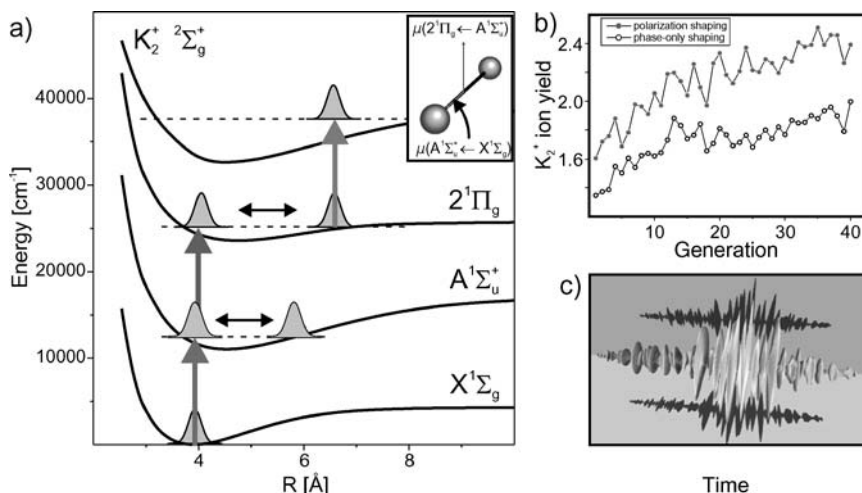
Figure 7 (*a*) Excitation scheme for the multiphoton ionization of potassium dimers (K$_2$) at a wavelength of 785 nm. The pump pulse creates a wavepacket in the A$^1\Sigma_u^+$ state. With some probability, molecules in the A$^1\Sigma_u^+$ states are further excited to the $2^1\Pi_g$ state and ionized to the ionic K$_2^+$ $^2\Sigma_g^+$ state. The inset shows the transition dipole moment from the X$^1\Sigma_g^+$ ground state to the A$^1\Sigma_u^+$ state (parallel transition) and the transition dipole moment from the A$^1\Sigma_u^+$ state to the $2^1\Pi_g$ state (perpendicular transition). (*b*) Fitness curve for the optimization of the K$_2^+$ ion yield relative to the unshaped values. The *open black circles* show the results for the polarization optimization, whereas the gray disks indicate the values for phase-only shaping. (*c*) Three-dimensional representation of polarization state and the instantaneous frequency of the optimal laser pulse. Time evolves from -1.5 ps (*left*) to $+1.5$ ps (*right*).

product yield is achieved. The time-dependent polarization state along with the instantaneous frequency of the reconstructed pulse is displayed in Figure 7*c*. This demonstrates that complex pulse shapes in terms of phase and polarization state result from the optimization process when the molecular dynamics and the polarization state are coupled. The results demonstrate that time-dependent shaping of femtosecond light polarization gives access to a further level of control of quantum systems. Less optimization was found in the phase-only optimization of the K$_2^+$ yield, which proves the importance of simultaneous control of the polarization state.

4. QUANTUM CONTROL IN THE STRONG FIELD LIMIT

4.1. Quantum Control with Intense Femtosecond Pulse Sequences on Atoms

Numerous quantum control schemes have been proposed and successfully demonstrated, and these are reviewed in recent monographs (13, 14). Most of these—for example the Brumer-Shapiro scheme (90), the Tannor-Kosloff-Rice scheme (91),

or techniques based on (higher-order) spectral interference (92, 93)—are operative in the weak-field regime. However, a few powerful strong-field quantum control schemes [Rapid Adiabatic Passage (RAP) and Stimulated Raman Adiabatic Passage (STIRAP) (94–96), and the modification of the potential surfaces (97, 98)] were demonstrated as well. An alternative approach makes use of the combination of pulse-shaping techniques (83, 99–101) with adaptive feedback-learning loops. This technique allows optimization of virtually any conceivable observable (20, 102–112) with enormous success. However, in many cases it is nearly impossible to identify the underlying physical mechanism from the electrical fields obtained by this procedure. In order to better understand optimal control experiments, our approach is based on the investigation of quantum control on a simple well-defined model system excited by well-characterized intense phase-modulated laser pulses.

In this section, we investigate the quantum control of the photo-ionization of potassium atoms exerted by an intense laser pulse sequence. The K $4p \leftarrow 4s$ transition is coherently excited and probed via two-photon ionization from the $4p$ state. The resulting photoelectrons are detected with energy resolution. Because the laser carrier frequency is close to the $4p \leftarrow 4s$ resonance, the atom is treated as a two-level system.

Figure 8a shows the excitation scheme used in this experiment. Unlike conventional pump-probe scenarios in which the first pump pulse initiates the dynamics that is probed by the second pulse, in our experiment the same pulse is used to drive the neutral dynamics and to trigger the ionization. Because the neutral-to-ionic transitions are much weaker than the K $(4p \leftarrow 4s)$ transition, the photo-ionization is described using perturbation theory. The amplitudes $c(E)$ for the ionization from the $4p$ excited state read (113–115)

$$c(E) \sim \int\limits_{-\infty}^{\infty} dt \ C_b(t) \ W^2(t) \ e^{i(E+E_{IP}-E_{4p})t/\hbar}, \qquad 30.$$

where $C_b(t)$ describes the time-dependent excited state $(4p)$ amplitude. From Equation 30, the amplitudes $c(E)$ are the Fourier transform of the excited state amplitude $C_b(t)$ windowed by the square of the electrical field (times dipole moments) $W^2(t)$. As a consequence, the quantum mechanical phase information of the excited state amplitudes is preserved to some extent in the photoelectron spectrum. Similar to the modification of the laser pulse shape in the time domain by phase modulation in the frequency domain, the shape of the photoelectron spectrum $|c(E)|^2$ is modified by the temporal phase of the amplitude $C_b(t)$. The simultaneous excitation/ionization technique therefore permits the use of photoelectron spectra as a fingerprint of the quantum mechanical phase imparted by the interaction with the shaped laser pulse. In passing, we note that similar effects are also present in molecular systems, although the vibrational dynamics tends to obscure the interference fringes (113, 116, 117).

The potential of phase locked pulse sequences as a novel spectroscopic tool was demonstrated on single photon molecular transitions (118). Later, weak field
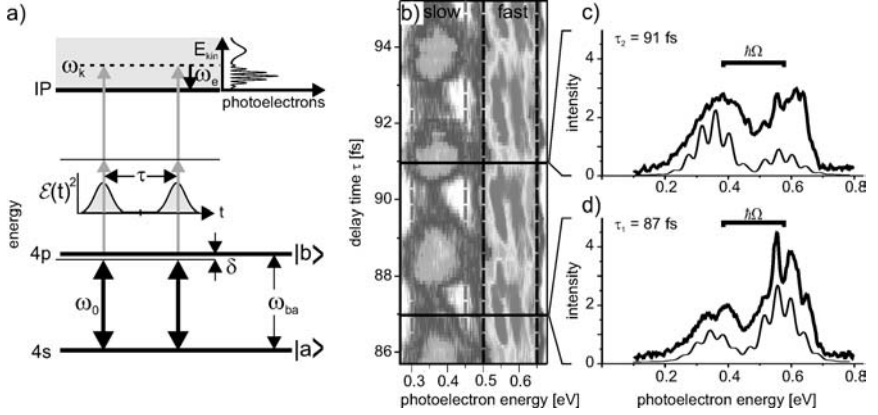
Figure 8 (*a*) Energy level diagram for excitation of K atoms. A sequence of two time-delayed (τ) 30 fs FWHM laser pulses with an intensity envelope $\mathcal{E}^2(t)$ and a carrier frequency ω_0 (corresponding to 785 nm) detuned from the resonance frequency ω_{ba} (768 nm) create a coherent superposition of the lower 4*s* ($|a\rangle$) and the upper 4*p* ($|b\rangle$) states of K atoms (*black arrows*). Photoelectrons with a kinetic energy $E_{kin} = \hbar\omega_e$ from simultaneous two-photon ionization (*gray arrows*) of the 4*p* state to the continuum (ω_k) are measured. (*b*) Experimental photoelectron spectra as a function of the delay time τ at a fixed laser intensity of I_0 (0.54×10^{12} W/cm^2). Note that the slow and fast electrons are out of phase. Sections along the energy axes yield measured photoelectron spectra (*bold*) at $\tau_2 = 91.0$ fs (*c*) and $\tau_1 = 87.0$ fs (*d*). Simulated spectra for the respective delay times τ_1 and τ_2 convoluted with 25 meV spectrometer resolution are given for comparison. The Autler-Townes splitting $\hbar\Omega$ is indicated with *horizontal bars*.

pulse sequences were employed in order to control multiphoton transitions of atoms (114, 118a, 119–121) and solid-state samples (122, 123). Subtle differences due to the relative optical phase produced either by optical phase shifts or time delay (124) can control the outcome of the experiment. Although the experiments were mostly interpreted in terms of quantum interference, another explanation of the weak field experimental results can be given in terms of (higher-order) spectral interference, i.e., by the analysis of the nth order spectrum of the pulse

$$\widetilde{E^n}(\omega) = \int\limits_{-\infty}^{\infty} E^n(t) \, e^{i\omega t} dt. \qquad \qquad 31.$$

In contrast, in this section we discuss the strong field excitation of the (4*p* $\leftarrow$ 4*s*) transitions of potassium atoms with phase-locked pulses. The experimental set-up is described in Reference (125) and sketched in Figure 8. Panel *b* shows a gray scale representation of the photoelectron spectra as a function of the delay time τ. Because of the high laser intensity, the photoelectron spectrum is split into the Autler-Townes (AT) doublet (126). Experimental photoelectron spectra are

shown in Figure 8c and 8d, and compared to (off-resonant) simulations. The fast (0.6 eV) and the slow (0.35 eV) AT components are out of phase by half a transition period ($\approx$1.3 fs). Moreover, the photoelectron spectra at $\tau = 87$ fs (Figure 8d) and $\tau = 91$ fs (Figure 8c) exhibit pronounced differences. For instance, at $\tau = 87$ fs, the high-energy photoelectrons are more intense and show interference structures.

We analyze the experimental observations in light of standard two-level physical pictures, i.e., the bare state population, the dressed state population, and the dynamics of the Bloch vector (95, 96, 127). Because the observed photoelectron spectra are periodically reproduced every transition period upon variation of the delay, we discuss the physical mechanism for a typical example. Figure 9 shows the model calculations for an idealized resonant two-level model.

Figure 9a shows the instantaneous Rabi frequency $\Omega(t)$ and the temporal optical phase function $\chi(t)$ for two pulses with the pulse area of $\theta = \frac{7\pi}{2}$ each, separated by $\tau = 146.7$ fs. Because of the delay, the optical phase jumps by $\frac{\pi}{2}$ in between the two pulses. The time evolution of the excited state population is depicted in Figure 9b. The first pulse shows Rabi oscillations but, surprisingly, the population is frozen during the interaction of the atom with the second intense resonant laser pulse. The physical effect of the second pulse is most clearly seen in the complex representation (Figure 9e). During the second pulse, both quantum mechanical amplitudes C_a and C_b rotate clockwise on a circle (see *open arrows* in Figure 9e). Therefore the population is constant during the second pulse, but the quantum mechanical phase is manipulated during this pulse. A very intuitive picture of the dynamics is obtained from the Bloch sphere perspective. The first pulse prepares a coherent superposition, i.e., after the first pulse the Bloch vector ρ points in the $+v$ direction. The optical phase controls the position of the angular velocity vector (see optical phase in Figure 9f). Because of an optical phase of $\chi = \frac{\pi}{2}$, the angular velocity vector Ω_B is aligned parallel to ρ. Because the equation of motion for the Bloch vector during the second pulse reads $\dot{\rho}(t) = \Omega_B \times \rho(t)$, the Bloch vector is trapped, implying a constant population because the w component of the Bloch vector $w = |C_b|^2 - |C_a|^2 = \frac{1}{2}$ is constant. There is a general relation of the Bloch vector motion and the population of a dressed state: Whenever the vectors $\rho(t)$ and Ω_B are parallel and antiparallel the atom is in the upper and lower dressed state, respectively. Because the quantum mechanical phase is mapped by the photoelectron spectrum, this uncommon dynamics translates into a unique photoelectron spectrum. As seen in Figure 9g, the low-energy photoelectrons are reduced in intensity and show no internal structure, whereas the high-energy photoelectrons are enhanced and display interference fringes. Figure 9c shows that during the second pulse only the upper dressed state is populated in accordance with the vectors Ω_B, and $\rho(t)$ is parallel during the second laser pulse. This is an example of the selective population of a single dressed state prepared by a two-pulse sequence via pure phase control.

We believe that the selective population of dressed states is an important physical mechanism for the control of larger molecules as well. For example, a chemical reaction with the possible outcome A and B might by controlled by the population of some intermediate resonant state. Generally, if we excite the system with
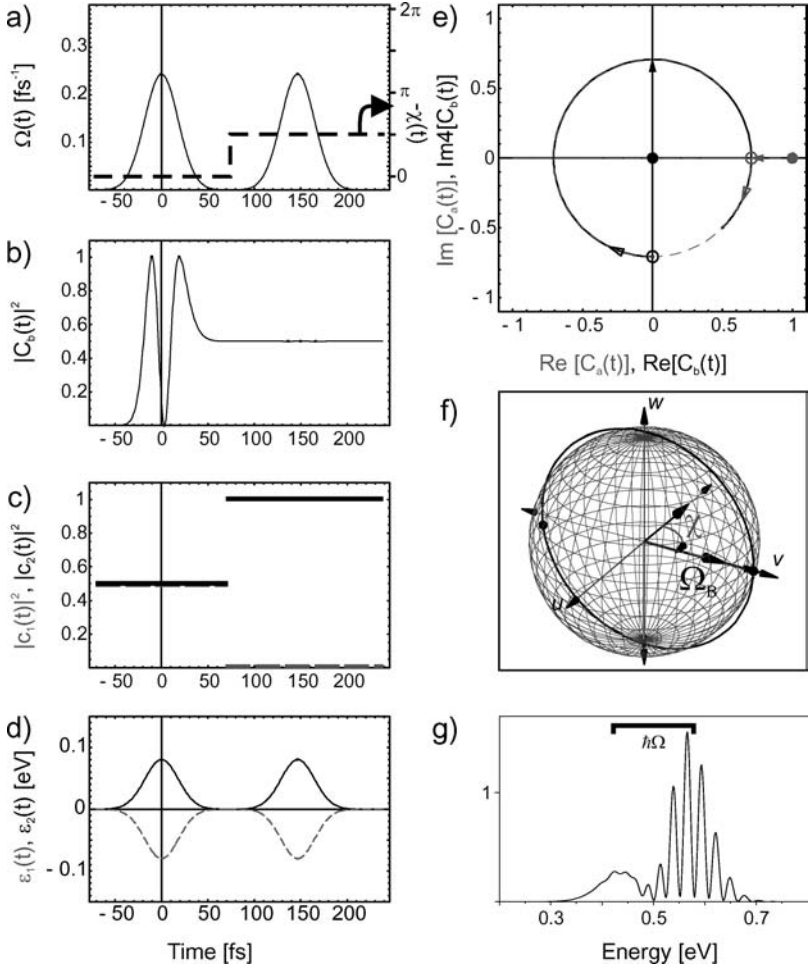
Figure 9 Excitation of ground state atoms with a pulse sequence of *FWHM* = 30 fs pulse duration and $\theta = \frac{7\pi}{2}$ pulse area. (*a*) Shows the envelope of the laser field $\hbar\Omega(t) = \mu\mathcal{E}(t)$ and the optical phase function $\chi(t)$; (*b*) the time evolution of the upper state population $C_b(t)$; (*c*) the population of the upper and lower dressed state in *black* and *gray*, respectively; (*d*) the eigenenergies of the dressed states; and (*e*) the parametric representation of the complex amplitudes of the excited state [$C_b(t)$; *black*] and the ground state [$C_a(t)$; *gray dashed*], where the *disks* indicate the initial amplitudes, *filled arrows* the direction of motion during the first pulse, *open circles* the initial amplitudes for the second pulse, and *open arrows* the direction of motion during the second pulse. (*f*) Shows the trace of the Bloch vector and the angular velocity vector at the peak intensity (*black*, first pulse; *gray*, second pulse) and the optical phase χ_2. The initial Bloch vector and the Bloch vector for the state prepared by the first pulse are shown in addition. *Little spheres* indicate the orientation of the Bloch vector motion. (*g*) The photoelectron spectrum with the Autler-Townes splitting $\hbar|\Omega|$.
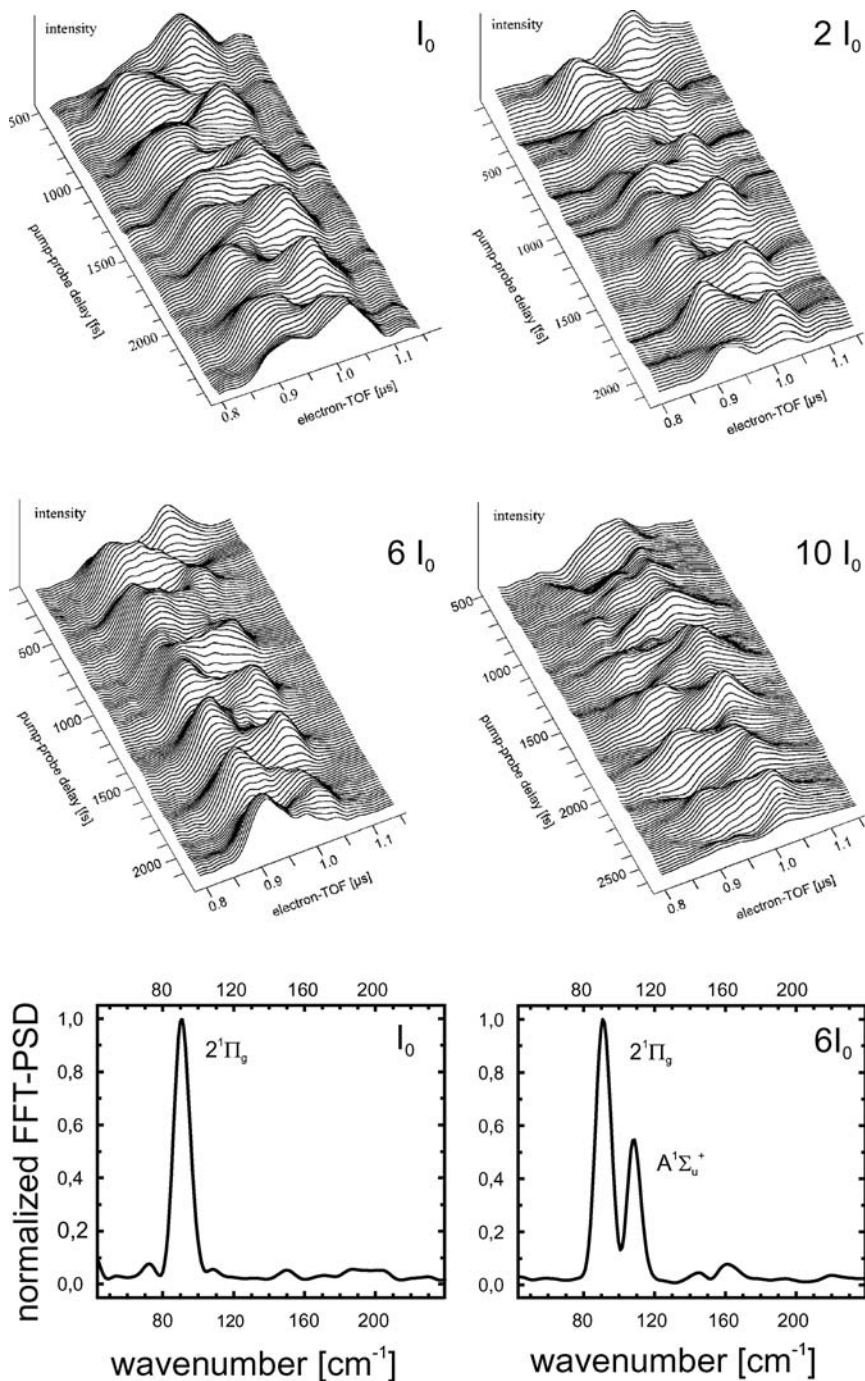
bandwidth-limited pulses we are not able to exert control over the population of the corresponding dressed states, leading to a constant branching ratio of A and B. If we were able to control the decisive step, the outcome will be the selective production of either A or B depending on our ability to control the population of the dressed states.

4.2. Light-Induced Potentials

In Section 2 we have shown that TRPE-spectra are an ideal tool to monitor changes of radial probability densities as a function of time in the weak field limit. Regarding, again, the sodium dimer transitions as sketched in Figure 3, we now consider the wavepacket motion after a pump-pulse of intensity I_0 has interacted with the system and investigate strong field probe-pulse ionization. Here we present a somewhat simplified picture; for a thorough discussion, see Bandrauk (128).

Because the probe-pulse transition from the Π-state into the continuum may be still described within the weak field regime, the effects to be expected take place within the neutral manifold of electronic states. The Schrödinger equation for the nuclear motion in the lower three electronic states, upon neglect of the kinetic energy operators (see Section 2.3) and performance of the unitary transformation

$$(\tilde{\psi}_X, \tilde{\psi}_A, \tilde{\psi}_\Pi) = \left(e^{-i\omega_2 t}\psi_X, \psi_A, e^{i\omega_2 t}\psi_\Pi\right), \qquad 32.$$

reads

$$i\hbar\frac{\partial}{\partial t}\begin{pmatrix}\tilde{\psi}_X \\ \tilde{\psi}_A \\ \tilde{\psi}_\Pi\end{pmatrix} = \begin{pmatrix} V_X + \hbar\omega_2 & -f_2(t)/2 & 0 \\ -f_2(t)/2 & V_A & -f_2(t)/2 \\ 0 & -f_2(t)/2 & V_\Pi - \hbar\omega_2 \end{pmatrix}\begin{pmatrix}\tilde{\psi}_X \\ \tilde{\psi}_A \\ \tilde{\psi}_\Pi\end{pmatrix}, \qquad 33.$$

where the counter-rotating wave terms are not taken into account and we set all projections of the transition dipole moments on the laser polarizations to unity.

The approximate Hamilton matrix in Equation 33 contains shifted potentials that cross each other at positions where

$$V_A(R) - V_X(R) - \omega_2 = 0 \qquad\qquad 34.$$

$$V_\Pi(R) - V_A(R) - \omega_2 = 0. \qquad\qquad 35.$$

Figure 10   (*Upper*) Time-of-flight photoelectron distributions for a fixed pump laser intensity ($I_0 \approx 10^{11}$ W/cm^2) and increasing probe laser intensity; $I_{probe} = I_0$, 2 I_0, 6 I_0 and 10 I_0. The wavepacket dynamics on the neutral electronic states is mapped. (*Lower*) Cuts of FFT spectra at the outer turning point of the wavepacket at a pump laser intensity of I_0 (*left*) and 6 I_0 (*right*). The contribution of the $A^1\Sigma_u^+$ wavepacket starts to appear at intermediate intensities and increases rapidly with increasing laser intensity. This behavior is attributed to the effect of perturbed molecular potentials in high laser fields (light-induced potentials).

The latter conditions are identical to the resonance conditions for an electronic transition as obtained in the weak field limit (see Section 2): If the difference potential equals the laser frequency, because of the off-diagonal field coupling, a transition between the different states is induced at a well-defined value of the bondlength R. This picture is valid in the weak field regime where the (diabatic) potential matrix is approximately diagonal. However, if the field intensity is increased, the off-diagonal elements containing the field amplitudes become substantial. It is then advantageous to switch to the adiabatic potential matrix resulting from diagonalization of the diabatic matrix. The so obtained R-dependent light-induced potentials exhibit avoided crossings, i.e., they are strongly modified around the crossing regions. They are very helpful to understand phenomena like bond hardening or bond softening (44, 129, 130) and also, as we showed for the Na$_2$ molecule, to analyze the photodissociation occurring upon high-intensity multiphoton ionization (131). In general, many potential curves are involved here as multiple photon absorption becomes more probable with increasing intensity (128, 132). As mentioned before, this is not included here. Concerning the photoelectron spectra, visible effects are to be expected because at different times, when the vibrational wavepackets in the various states are located around different bond lengths, a light-induced modification of the resonance conditions may enhance or suppress ionization paths in the multiphoton process. This indeed can be seen in Figure 10. The recorded photoelectron spectra are depicted for a fixed pump-pulse intensity I_0 of approximately 10^{11} W/cm^2 and various probe-pulse intensities, as indicated (97). Obviously, the spectra and their dynamical features are quite sensitive to the intensity variations. The lower part of Figure 10 shows the Fourier transforms taken at a fixed electron energy and for two intensities. The energy corresponds to the location of the $2^1\Pi_g$-state vibrational wavepacket at its outer turning point. As expected from the resonance condition equation (Equation 16) valid in the weak field limit, for the lower intensity a single peak corresponding to the $2^1\Pi_g$ frequency is seen. Increasing the intensity to $6\,I_0$ results in a second peak that corresponds to the $A^1\Sigma_u^+$ frequency. It is important to notice that this contribution is not due to a nonresonant two-photon ionization out of the $A^1\Sigma_u^+$ state; rather, here we find a resonance-enhanced contribution that can be explained with the picture of light-induced potentials described above (22, 97).

The results presented in this subsection illustrate that the transient perturbation of the molecular electronic structure by intense fields can be directly traced via TRPES, and that the field intensity can be used as a control parameter to close and open ionization pathways that are not accessible in the weak field regime.

5. CONCLUSION

This review reports on femtosecond photoelectron spectroscopy applied to atoms and small molecules with regard to quantum control. The examples from our work show that this technique is able to provide direct insight into quantum

mechanical effects induced by the interaction of matter with weak and also strong ultrashort laser pulses. This is particularly important if intense and shaped laser fields are employed. Identifying the underlying quantum dynamics on computable small systems helps to unravel the adaptive control experiments on large systems. In particular, the insights obtained by these methods may be transferred to general applications in quantum control. Applying angular resolved photoelectron spectroscopy together with pulse-shaping techniques on aligned samples will open up new perspectives for identifying control mechanisms in the future.

ACKNOWLEDGMENTS

The *Annual Review of Physical Chemistry* is online at
http://physchem.annualreviews.org

LITERATURE CITED

1. *Picosecond Phenomena, Ultrafast Phenomena, Springer Ser. Chem. Phys. I-XII*, Vols. 4, 14, 23, 38, 46, 48, 53, 55, 60, 62, 63, 66. Heidelberg: Springer-Verlag

2. Kaiser W, ed. 1993. *Ultrashort Laser Pulses*. Heidelberg: Springer-Verlag

3. Zewail AH. 1994. *Femtochemistry*, Vols. I, II. Singapore: World Sci.

4. Wöste LW, Manz J, eds. 1995. *Femtosecond Chemistry*, Vols. I, II. Weinheim: VCH

5. Chergui M, ed. 1996. *Femtochemistry—Ultrafast Chemical and Physical Processes in Molecular Systems*. Singapore: World Sci.

6. Sundström V, ed. 1996. *Femtochemistry and Femtobiology: Ultrafast Reaction Dynamics at Atomic-Scale Resolution*. London: Imperial Coll. Press

7. Schryver FD, DeFeyter S, Schweitzer G, eds. 2001. *Femtochemistry*. Weinheim: Wiley-VCH

8. Douhal A, Santamaria J, eds. 2002. *Femtochemistry and Femtobiology*. Singapore: World Sci.

9. Martin M, Hynes JT, eds. 2004. *Femtochemistry and Femtobiology: Ultrafast Events in Molecular Science*. Oxford: Elsevier

10. Hannaford P, ed. 2004. *Femtosecond Laser Spectroscopy, Kluwer Ser. Prog. Lasers*. Dordrecht: Kluwer Acad.

11. Zewail AH. 2000. *J. Phys. Chem.* 104: 5660–94

12. Zewail AH. 2000. *Angew. Chem. Int. Ed. Engl.* 39:2587–631

13. Rice SA, Zhao M. 2000. *Optical Control of Molecular Dynamics*. New York: Wiley-Intersci.

14. Shapiro M, Brumer P. 2003. *Principles of the Quantum Control of Molecular Processes*. Hoboken, NJ: Wiley-Intersci.

15. Warren WS, Rabitz H, Dahleh M. 1993. *Science* 259:1581–69

16. Baumert T, Helbing J, Gerber G, Wöste L,

Zewail AH, et al. 1997. *Adv. Chem. Phys.* 101:47–82 [note]

17. Gordon RJ, Rice SA. 1997. *Annu. Rev. Phys. Chem.* 48:601–41
18. Rabitz H, de Vivie-Riedle R, Motzkus M, Kompa KL. 2000. *Science* 288:824–28
19. Gordon RJ, Zhu LC, Seideman T. 1999. *Acc. Chem. Res.* 32:1007–16
20. Brixner T, Gerber G. 2003. *Chem. Phys. Chem.* 4:418–38
21. Dantus M, Lozovoy VV. 2004. *Chem. Rev.* 104:1813–59
22. Brixner T, Pfeifer T, Gerber G, Wollenhaupt M, Baumert T. 2004. See Ref. 10, pp. 229–71
23. Materny A, Chen T, Schmitt M, Siebert T, Vierheilig A, et al. 2000. *Appl. Phys. B* 71:299–317
24. Dantus M. 2001. *Annu. Rev. Phys. Chem.* 52:639–79
25. Neumark DM. 2001. *Annu. Rev. Phys. Chem.* 52:255–77
26. Stolow A. 2003. *Annu. Rev. Phys. Chem.* 54:89–119
27. Stolow A. 2003. *Int. Rev. Phys. Chem.* 22:377–405
28. Stolow A, Bragg AE, Neumark DM. 2004. *Chem. Rev.* 104:1719–57
29. Nuguent-Glandorf L, Scheer M, Samuels DA, Bierbaum VM, Leone SR. 2002. *J. Chem. Phys.* 117:6108–16
30. Manz J. 1996. In *Femtochemistry and Femtobiology: Ultrafast Reaction Dynamics at Atomic-Scale Resolution*, ed. V Sundström, pp. 80–319. London: Imperial Coll. Press
31. Stock G, Domcke W. 1997. *Adv. Chem. Phys.* 100:1–169
32. Mukamel S. 1995. *Principles of Nonlinear Optical Spectroscopy*. New York: Oxford Univ. Press
33. Reid KL. 2003. *Annu. Rev. Phys. Chem.* 54:397–424
34. Davies JA, Continetti RE, Chandler DW, Hayden CC. 2000. *Phys. Rev. Lett.* 84:5983–86
35. Matsumoto Y, Kim SK, Suzuki T. 2003. *J. Chem. Phys.* 119:300–3

36. Seideman T. 1997. *J. Chem. Phys.* 107:7859–68
37. Arasaki Y, Takatsuka K, Wang K, McKoy V. 1999. *Chem. Phys. Lett.* 302:363–74
38. Takatsuka K, Arasaki Y, Wang K, McKoy V. 2000. *Faraday Discuss.* 115:1–15
39. Seideman T. 2001. *Phys. Rev. A* 64:042504
40. Seideman T. 2002. *Annu. Rev. Phys. Chem.* 53:41–65
41. Seel M, Domcke W. 1991. *J. Chem. Phys.* 95:7806–22
42. Seel M, Domcke W. 1991. *Chem. Phys.* 151:59–72
43. Agostini P, Fabre F, Mainfray G, Petite G, Rahman NK. 1979. *Phys. Rev. Lett.* 42:1127–30
44. Zavriyev A, Bucksbaum PH, Muller HG, Schumacher DW. 1990. *Phys. Rev. A* 42:5500–13
45. Diels JC, Rudolph W. 1996. *Ultrashort Laser Pulse Phenomena*. San Diego: Academic
46. Wollenhaupt M, Assion A, Baumert T. 2005. In *Springer Handbook of Lasers and Optics*, ed. F Träger. Heidelberg: Springer-Verlag. In press
47. Ermoshin VA, Engel V. 2001. *Eur. Phys. J. D* 15:413–22
48. Gräfe S, Scheidel D, Henriksen NE, Møller K, Engel V. 2004. *J. Phys. Chem.* 108:8954–60
49. Mulliken RS. 1971. *J. Chem. Phys.* 55:309–14
50. Baumert T, Bühler B, Grosser M, Thalweiser R, Weiss V, et al. 1991. *J. Phys. Chem.* 95:8103–10
51. Assion A, Geisler M, Helbing J, Seyfried V, Baumert T. 1996. *Phys. Rev. A* 54:4605–8
52. Davisson C, Germer L. 1927. *Phys. Rev.* 30:705–40
53. De Broglie L. 1925. *Ann. Phys. Fr.* 3:22–128
54. Marton L. 1952. *Phys. Rev.* 85:1057–58
55. Ihee H, Lobastov VA, Gomez UM, Godson BM, Srinivasan R, et al. 2001. *Science* 291:458–462

56. Bhardwaj VR, Rayner DM, Villeneuve DM, Corkum PB. 2001. *Phys. Rev. Lett.* 87:253003

57. Wollenhaupt M, Assion A, Liese D, Sarpe-Tudoran C, Baumert T, et al. 2002. *Phys. Rev. Lett.* 89:173001

58. Lein M, Erdmann M, Engel V. 2000. *J. Chem. Phys.* 113:3609–14

59. Skovsen E, Stapelfeldt H, Juhl S, Moelmer K. 2003. *Phys. Rev. Lett.* 91: 090406

60. Meier C, Engel V. 1993. *Chem. Phys. Lett.* 212:691–718

61. Frohnmeyer T, Baumert T. 2000. *Appl. Phys. B* 71:259–66

62. Ermoshin VA, Engel V, Meier C. 2000. *J. Chem. Phys.* 113:5770–75

63. Shen Z, Boustani I, Erdmann M, Engel V. 2001. *Chem. Phys. Lett.* 339:362–68

64. Shen Z, Engel V. 2002. *Chem. Phys. Lett.* 358:344–49

65. Meier C, Engel V. 2002. *Phys. Chem. Chem. Phys.* 4:5014

66. Schwoerer H, Pausch R, Heid M, Engel V, Kiefer W. 1997. *J. Chem. Phys.* 107:9749–54

67. Nicole C, Bouchène MA, Meier C, Magnier S, Schreiber E, Girard B. 1999. *J. Chem. Phys.* 111:7857–64

68. Andersson R, Kadi M, Davidsson J, Hansson T. 2002. *Chem. Phys. Lett.* 352:106–12

69. Pesce L, Amitay Z, Uberna R, Leone SR, Ratner M, Kosloff R. 2001. *J. Chem. Phys.* 114:1259–71

70. Lohmüller T, Erdmann M, Rubner O, Engel V. 2003. *Eur. Phys. J. D* 25:95–99

71. Valance A, Nguyen Tuan Q. 1982. *J. Phys. B* 15:17–33

72. Vergès J, Effantin C, d'Incan J, Cooper DL, Barrow RF. 1984. *Phys. Rev. Lett.* 53:46–47

73. Cooper DL, Barrow RF, Vergès J, Effantin C, d'Incan J. 1984. *Can. J. Phys.* 62:1543–62

74. Assion A, Baumert T, Seyfried V, Weiss V, Wiedenmann E, Gerber G. 1996. *Z. Phys. D* 36:265–71

75. Assion A, Baumert T, Geisler M, Seyfried V, Gerber G. 1998. *Eur. Phys. J. D* 4:145–49

76. Wollenhaupt M, Assion A, Bazhan O, Liese D, Sarpe-Tudoran C, Baumert T. 2002. *Appl. Phys. B* 74:121–25

77. Wollenhaupt M, Assion A, Graefe O, Liese D, Sarpe-Tudoran C, et al. 2003. *Chem. Phys. Lett.* 376:457–64

78. Meyer S, Meier C, Engel V. 1998. *J. Chem. Phys.* 108:7631–36

79. Assion A, Baumert T, Helbing J, Seyfried V, Gerber G. 1996. *Chem. Phys. Lett.* 259:488–94

80. Lohmüller T, Erdmann M, Engel V. 2003. *Chem. Phys. Lett.* 373:319–36

81. Child MS. 1996. *Molecular Collision Theory*. Mineola, NY: Dover

82. Ballard JB, Stauffer HU, Mirowski E, Leone SR. 2002. *Phys. Rev. A* 66:043402

83. Weiner AM. 2000. *Rev. Sci. Instr.* 71: 1929–60

84. Brixner T, Gerber G. 2001. *Opt. Lett.* 26:557–59

85. Brixner T, Krampert G, Niklaus P, Gerber G. 2002. *Appl. Phys. B* 74:133–44

86. Oron D, Dudovich N, Silberberg Y. 2003. *Phys. Rev. Lett.* 90:213902

87. Oron D, Dudovich N, Silberberg Y. 2004. *Phys. Rev. Lett.* 92:103003

88. Suzuki T, Minemoto S, Kanai T, Sakai H. 2004. *Phys. Rev. Lett.* 92:133005

89. Brixner T, Krampert G, Pfeifer T, Selle R, Gerber G, et al. 2004. *Phys. Rev. Lett.* 92:208301

90. Brumer P, Shapiro M. 1986. *Chem. Phys. Lett.* 126:541–64

91. Tannor DJ, Kosloff R, Rice SA. 1986. *J. Chem. Phys.* 85:5805–20

92. Meshulach D, Silberberg Y. 1998. *Nature* 396:239–42

93. Lozovoy VV, Pastirk I, Walowicz A, Dantus M. 2003. *J. Chem. Phys.* 118:3187–96

94. Gaubatz U, Rudecki P, Schiemann S, Bergmann K. 1990. *J. Chem. Phys.* 92: 5363–76

95. Vitanov NV, Halfmann T, Shore BW,

Bergmann K. 2001. *Annu. Rev. Phys. Chem.* 52:763–809

96. Goswami D. 2003. *Phys. Rep.* 374:385–481

97. Frohnmeyer T, Hofmann M, Strehle M, Baumert T. 1999. *Chem. Phys. Lett.* 312:447–54

98. Niikura H, Corkum PB, Villeneuve DM. 2003. *Phys. Rev. Lett.* 90:20361

99. Weiner AM, Heritage JP, Kirschner EM. 1988. *J. Opt. Soc. Am. B* 5:1563–72

100. Weiner AM, Leaird DE, Wiederrecht GP, Nelson KA. 1990. *Science* 247:1317–19

101. Weiner AM, Leaird DE, Patel JS, Wullert JR. 1990. *Opt. Lett.* 15:326–28

102. Judson RS, Rabitz H. 1992. *Phys. Rev. Lett.* 68:1500–3

103. Baumert T, Brixner T, Seyfried V, Strehle M, Gerber G. 1997. *Appl. Phys. B* 65:779–82

104. Bardeen CJ, Yakolev VV, Wilson KR, Carpenter SD, Weber PM, Warren WS. 1997. *Chem. Phys. Lett.* 280:151–58

105. Assion A, Baumert T, Bergt M, Brixner T, Kiefer B, et al. 1998. *Science* 282:919–23

106. Bartels R, Backus S, Christov I, Kapteyn H, Murnane M. 2001. *Chem. Phys.* 267:277–89

107. Feurer T, Glaß A, Rozgonyi T, Sauerbrey R, Szabo G. 2001. *Chem. Phys.* 267:223–29

108. Herek JL, Wohlleben W, Cogdell R, Zeidler D, Motzkus M. 2002. *Nature* 417:533–35

109. Degert J, Wohlleben W, Chatel B, Motzkus M, Girard B. 2002. *Phys. Rev. Lett.* 89:203003

110. Weinacht TC, Bartels R, Backus S, Bucksbaum PH, Pearson B, et al. 2001. *Chem. Phys. Lett.* 344:333–38

111. Levis RJ, Rabitz H. 2002. *J. Phys. Chem.* 106:6427–44

112. Daniel C, Full J, González L, Lupulescu C, Manz J, et al. 2003. *Science* 299:536

113. Meier C, Engel V. 1994. *Phys. Rev. Lett.* 73:3207–10

114. Meshulach D, Silberberg Y. 1999. *Phys. Rev. A* 60:1287–92

115. Bebb HH, Gold A. 1966. *Phys. Rev.* 143:1–24

116. Meier C, Engel V. 1996. See Ref. 5, pp. 667–70

117. Sun Z, Lou N. 2003. *Phys. Rev. Lett.* 91:023002

118. Scherer NF, Carlson RJ, Matro A, Du M, Ruggiero AJ, et al. 1991. *J. Chem. Phys.* 95:1487–511

118a. Präkelt A, Wollenhaupt M, Sarpe-Tudoran C, Baumert T. 2005. *Phys. Rev. A* 70:In press

119. Blanchet V, Nicole C, Bouchene MA, Girard B. 1997. *Phys. Rev. Lett.* 78:2716–19

120. Bouchene MA, Nicole C, Girard B. 2000. *Opt. Commun.* 6733:1–10

121. Hornung T, Meier R, Zeidler D, Kompa KL, Proch D, Motzkus M. 2000. *Appl. Phys. B* 71:277–84

122. Heberle AP, Baumberg JJ, Köhler K. 1995. *Phys. Rev. Lett.* 75:2598–601

123. Petek H, Heberle AP, Nessler W, Nagano H, Kubota S, et al. 1997. *Phys. Rev. Lett.* 79:4649–52

124. Albrecht AW, Hybl JD, Faeder SMG, Jonas DM. 1999. *J. Chem. Phys.* 111:10934–56

125. Wollenhaupt M, Assion A, Bazhan O, Horn C, Liese D, et al. 2003. *Phys. Rev. A* 68:015401

126. Autler SH, Townes CH. 1955. *Phys. Rev.* 100:703–22

127. Allen L, Eberly JH. 1987. *Optical Resonance and Two-Level Atoms.* Mineola, NY: Dover

128. Bandrauk AD, ed. 1994. *Molecules in Laser Fields.* New York: Marcel Dekker

129. Bandrauk AD, Sink ML. 1981. *J. Chem. Phys.* 74:1110–17

130. Frasinski LJ, Posthumus JH, Plumridge J, Codling K, Taday PF, Langley AJ. 1999. *Phys. Rev. Lett.* 83:3625–28

131. Assion A, Baumert T, Weichmann U, Gerber G. 2001. *Phys. Rev. Lett.* 86:5695–98

132. Giusti-Suzor A, Mies FH, DiMauro LF, Charron E, Yang B. 1995. *J. Phys. B* 28:309–39